Journal of Power Sources 667 (2026) 239174

Contents lists available at ScienceDirect

Journal of Power Sources

journal homepage: www.elsevier.com/locate/jpowsour

Maximising lithium battery performance by capacity balancing: Determining the Pareto fronts for electrode thickness and porosity

Chikwesiri Imediegwu [a,b,c], Milo S.P. Shaffer [b,d], Mary P. Ryan [b], Ajit Panesar [a,*]

[a] Department of Aeronautics, South Kensington, Imperial College London, SW7 2AZ, UK
[b] Department of Materials, South Kensington, Imperial College London, SW7 2AZ, UK
[c] Department of Mechanical and Aerospace Engineering, University of Manchester, M13 9PL, UK
[d] Department of Chemistry, White City, Imperial College London, W12 0BZ, UK

HIGHLIGHTS

- Best electrode thickness and porosity under fast charge and discharge.
- Pareto-optimal balanced electrodes for high areal capacity and energy density.
- On the asymmetry of ion transport under fast charge and discharge.

ARTICLE INFO

Keywords:
Graphite
Full-cell modelling
Capacity balancing
Fast-charging

ABSTRACT

Effective battery design is complex, requiring the resolution of multiple conflicting demands. Even where optimal electrode thickness, porosity, and architecture have been determined for isolated electrodes, designing optimal electrode parameters in full-cell configurations remains challenging. The performances of the positive and negative electrodes are linked due to the need to balance their capacities and complicated by differing rate-limiting mechanisms and ion transport asymmetries, under charge and discharge. This work develops a rational strategy for full-cell electrode design. First, validated, physics-based continuum models are used to determine Pareto fronts identifying best target negative and positive electrode thickness and porosity, under charge and discharge. The calculated ion concentrations provide a mechanistic understanding of the charge/discharge asymmetry. These Pareto fronts are then plotted in the areal capacity-volumetric energy density plane to identify the most effective electrode combinations. The approach is illustrated for a lithium-ion cell configuration using a graphite negative electrode and a $LiNi_{0.6}Mn_{0.2}Co_{0.2}O_2$ positive electrode (Gr/NMC622) but can be generalised to other electrode pairs and battery chemistries.

1. Introduction

Lithium-ion (Li-ion) batteries are ubiquitous energy storage components, at different scales, within portable electronics (Wh), electrified transport (kWh) and large-scale renewable energy grids (MWh) [1,2]. There is a growing demand for increased capacity, cheaper, safer, fast-charging and long-life batteries, which has shaped the active reseamarch landscape [3–5]. In principle, practical cell capacity can be increased and costs reduced by increasing electrode thickness and decreasing the relative proportion of inactive cell components, such as the current collector and separator. However, the accompanying inefficiencies in ion transport limit the utilisation of the active material (AM), at higher charging rates and thicknesses, due to kinetic and concentration overpotentials which build across the electrode. Ion transport limitations can be alleviated by increasing the pore volume in the electrodes and adjusting its distribution to minimise tortuosity, giving more accessibility to the AM particles and hence better material utilisation, at a given rate. However, since these pores are filled with electrolyte, increasing porosity indirectly increases the mass of inactive electrolyte material, degrading the cell's specific capacity and gravimetric energy density. These factors lead to a trade-off between useable capacity and rate capability in battery design [6,7]. In addition, maximising material utilisation increases the chance of lithium plating and dendrite growth, particularly, during fast charge and discharge, if

* Corresponding author.
E-mail address: a.panesar@imperial.ac.uk (A. Panesar).

https://doi.org/10.1016/j.jpowsour.2025.239174
Received 4 September 2025; Received in revised form 18 December 2025; Accepted 21 December 2025
Available online 2 January 2026

overpotentials develop in different regions of the electrode. The multi-faceted challenges and inter-dependent considerations for choosing the thickness, porosity and architecture for both the positive and negative electrodes, are compounded by the need to balance their capacities at different rates, during both charge and discharge, to design a high-performance battery [8–10].

The standard slurry-cast process for electrode manufacturing applies a paste of active materials, carbon-based conductive additives, and a polymeric binder to metal foil current collectors using slot-die coating; after evaporation of the carrier solvent, the electrode is calendared to achieve the desired mechanical and electrical properties [6]. Despite widespread adoption, the process remains largely empirical relying on trial-and-error, hands-on expertise, and specialist industry know-how [11]. There is a push for manufacturing approaches that offer more microstructural control, for example, exploiting electrode material grading or patterning; despite established benefits, the full scope for improvement and hence the economic case for implementation are less clear [12,13]. Other significant experimental efforts have been made to improve Li-ion battery performance, ranging from the development of new anode and cathode materials with high theoretical capacity and high operation voltages [11,14–16], to new battery chemistries with exceptional energy densities such as Li-sulphur and Li-air batteries [17]. However, much is still to be done to narrow the gap between theoretical capacity and useable capacity in practical operation, in both new and established systems [18,19]. The effects of electrode thickness and porosity on the rate capability of electrodes have been widely studied; for example, Electrochemical Impedance Spectroscopy (EIS) [20,21] has shown that AM particle size and particle size distribution are critical to electrode performance, life and safety [22]. Both template and template-free approaches have been devised to reduce tortuosity in electrodes and to improve the ion-transport in thick electrodes [23]. However, these experimental approaches to innovative battery design can be costly and time-consuming, often requiring expensive materials, prototypes, and extensive testing setups. Therefore, physics-based numerical models of battery operation are attractive, expanding the knowledge on the underlying multi-physical processes and mechanisms that challenge existing electrode design and manufacturing techniques.

Numerical modelling for battery design, offers significant benefits if carefully parameterised and validated by experiment [24,25]. It involves approximating the electrochemical transport phenomena (ions and electrons) within the cell's multiple phases by time-dependent governing physics equations to predict the behaviour and performance of the cell. The Doyle-Fuller-Newman (DFN) continuum model (also known as the P2D model for its pseudo radial dimension and 1-spatial dimension) implements porous electrode theory and electrode reaction kinetics and is the foundation of many contemporary battery models [3]. The DFN model assumes a uniform distribution of spherical AM particles as well as a power law relationship between transport properties (diffusivity and conductivity) and the porosity. The pseudo-dimension approximates the variation of ion concentrations within each particle and diffusive processes are governed typically by Fick's law. Continuum models provide a means to evaluate electrochemical performance efficiently, approximate degradation mechanisms and explore the high dimensional electrode design space at low cost and rapid throughput [20,26]. Detailed reviews of battery modelling strategies as well as modifications to the DFN model, are available [3,27,28]. To improve cell design, the sensitivity of the cell performance metrics to electrode parameters have been evaluated [29,30] and models have been leveraged to understand the limiting factors in thick electrodes [31–33]. In previous work, we explored a parametric sweep of the electrode design variables and quantified performance improvements associated with electrode architecture control. The DFN models were adapted with an additional spatial dimension to yield a pseudo 3-dimensional half-cell model [34]. This initial model development focused only on half-cell models for a positive electrode in a Li-ion battery, identifying the optimum thickness and porosity as a function of discharge rate. The next step is to extend a similar approach to negative electrodes, and to consider both charge and discharge conditions. However, there then remains a challenge of how to optimise the combined performance of two electrodes in a full-cell configuration. Significant variations in theoretical capacity, charge/discharge profiles and overpotentials in both electrodes make balancing non-trivial. Typically, cell-balancing is performed at low to moderate C-rates where capacities are near-nominal and overpotentials are minimised [35]. The demerit of such low-rate cell-balancing is that the electrodes perform sub-optimally when operated at other charge and discharge rates [8,10]. For fast-charging applications, the electrodes must be balanced at elevated C-rates. However, such cell-balancing is complicated by kinetic, concentration and ohmic overpotentials that occur during faster charge or discharge rates. Reaction rates at electrode interphases with the electrolyte also differ at each electrode [36].

In this work, we leverage our previous work optimising thickness and architecture of an NMC622 cathode under discharge [34]. By extending our prior pseudo-3D half-cell modelling framework to encompass both NMC cathodes and graphite anodes within a full-cell configuration, this study introduces a novel framework for electrode balancing in Li-ion batteries, enabling the systematic exploration of performance trade-offs under realistic charge and discharge conditions at intermediate C-rates. To evaluate the performance of a complete full-cell configuration, we develop and validate a complementary half-cell model for a negative graphite electrode. The validated model presents a means to explore the performance fields (volumetric energy density and areal capacity) of a positive and negative electrode in a full-cell configuration. Performance maps are generated for each electrode under both charge and discharge conditions at a practical rate to reveal a Pareto-optimal front of high-performing electrodes [37]. The Pareto front represents the set of best possible trade-offs between competing objectives. Electrode designs along this front are optimally balanced to perform well on both performance metrics; neither metric along the front can be improved without a loss in performance of the other. The approach aims to derive a high-performing full-cell configuration by balancing electrode capacities for both maximum total areal capacity and energy density.

2. Methodology

All half-cell models of this work are based on the Doyle-Fuller-Neumann (DFN) continuum framework [34]. These physics-based models enable the prediction of internal dynamics of key electrochemical variables inside the cell over time, including the evolution of the concentration of lithium ions in the liquid and solid phases, liquid and solid phase potentials and reaction rates at the interfaces of both phases. An Li/NMC622 half-cell configuration from previous work is used to study the performance of the positive electrode, and an Li/Gr (graphite) half-cell configuration is used for the negative electrode. NMC622 and graphite were chosen for their commercial availability and relevance in real-world applications, as well as the availability of experimental electrochemical data required to parameterise and validate models. Each electrode is assumed to be composed of a stochastic mixture of AM particles, conductive additives (5 % by volume) and binder material (5 % by volume). AM volume fractions are modelled to vary in the range (40 %–80 %) fully covering the realistic ranges typically applied (50 %–75 % in NMC cathodes [38] and 55 %–77 % in graphite anodes [39]), and extending slightly beyond such that performance limits are defined by underlying physical phenomena rather than artificially by chosen parameter range. The AM particles are assumed to be spherical and to be of uniform size. Therefore, diffusion in the radial (particle) dimension is modelled as spherically symmetric. All remaining pore spaces are assumed to be filled with electrolyte and convection in the electrolyte is assumed to be negligible. Transport properties are homogenised (averaged), derived as functions of the electrode porosity, based on Bruggeman relations. No mechanical or thermal considerations

are included and the diffusivity in the solid phase is assumed constant. The simulations focus on performance prediction and do not incorporate degradation mechanisms into the analyses, such as lithium plating and associated capacity fade [40,41]. These purely electrochemical continuum scale modelling equations and described in detail in previous work [34]. For completeness, the description of referenced experimental work, the validation of our negative electrode model as well as the model parameters for both electrodes are in the ESI. The computational models were developed and evaluated using the finite element software COMSOL Multiphysics. COMSOL provides a dedicated lithium-ion battery interface, enabling the definition of effective material properties for both solid and electrolyte phases within specific geometric domains. It facilitates the application of boundary conditions and resolves charge and mass conservation equations. A transient solver within COMSOL allows for the modelling of electrochemical transport phenomena, capturing the spatio-temporal evolution of solution variables of ion concentration, electronic and ionic potentials. Additionally, the software features high-fidelity meshing capability and a graphing interface for data visualisation. In this study, a single half-cell (dis)charge of a 60 X 60 mesh discretisation of the electrode region using square elements typically took 2–4 min on an Intel® Core™ i7-10710U CPU @ 1.10 GHz with a 32 GB RAM and six cores.

3. Results and discussion

3.1. Optimal thickness/porosity for electrodes under charge/discharge

In earlier work to study the capacity and rate capability of electrodes, half-cell models of an NMC622 cathode identified optimal electrode thicknesses and porosity that maximised volumetric energy density for a given discharge rate; volumetric energy density relates to gravimetric performance but is more readily interpreted from these models, and provides a more generalizable metric, as discussed previously [42]. The performance curve differed when the energy density was normalised by the total mass, including non-active materials. The corresponding active material volume fractions at these performance peaks provided a guide for designing application-specific high-performance positive electrodes. Here, we extend the study to electrode de-lithiation and to the negative electrode to determine optimal electrode parameters that are relevant to the design of a high-performing full-cell configuration. Plotting the areal capacity against the electrode thickness for different electrode porosities reveals a specific optimal electrode design for the peak performance, at a given C-rate, and is used as a performance metric in this work.

Consider the Li/NMC622 half-cells of Fig. 1a and e and their corresponding capacity-thickness curves (b) and (f) respectively under high rate. Though a high charge/discharge rate of 4C is exemplified here, qualitatively similar responses appear at all rates high enough to impose electrolyte concentration overpotentials. Under discharge, Li-ions intercalate into the positive electrode (it is lithiated). At this high discharge rate, the maximum areal capacity attained and the thickness at which it occurs varies with the AM volume fraction. The model identifies the optimal thickness ($\sim 85\mu m$) and AM volume fraction (0.4) to maximise useful areal capacity for a particular charge rate (4C, in the example shown) [20,42]. The opportunity to increase electrode thickness to improve areal capacity is limited, owing to underutilisation of the available AM. This phenomenology reflects the widely reported trade-off between electrode capacity and rate capability, arising from ion-transport inefficiencies and the build up of concentration and kinetic overpotentials. In the charge case of the same positive electrode (Fig. 1e–h) which only differs from the discharge case by the direction of

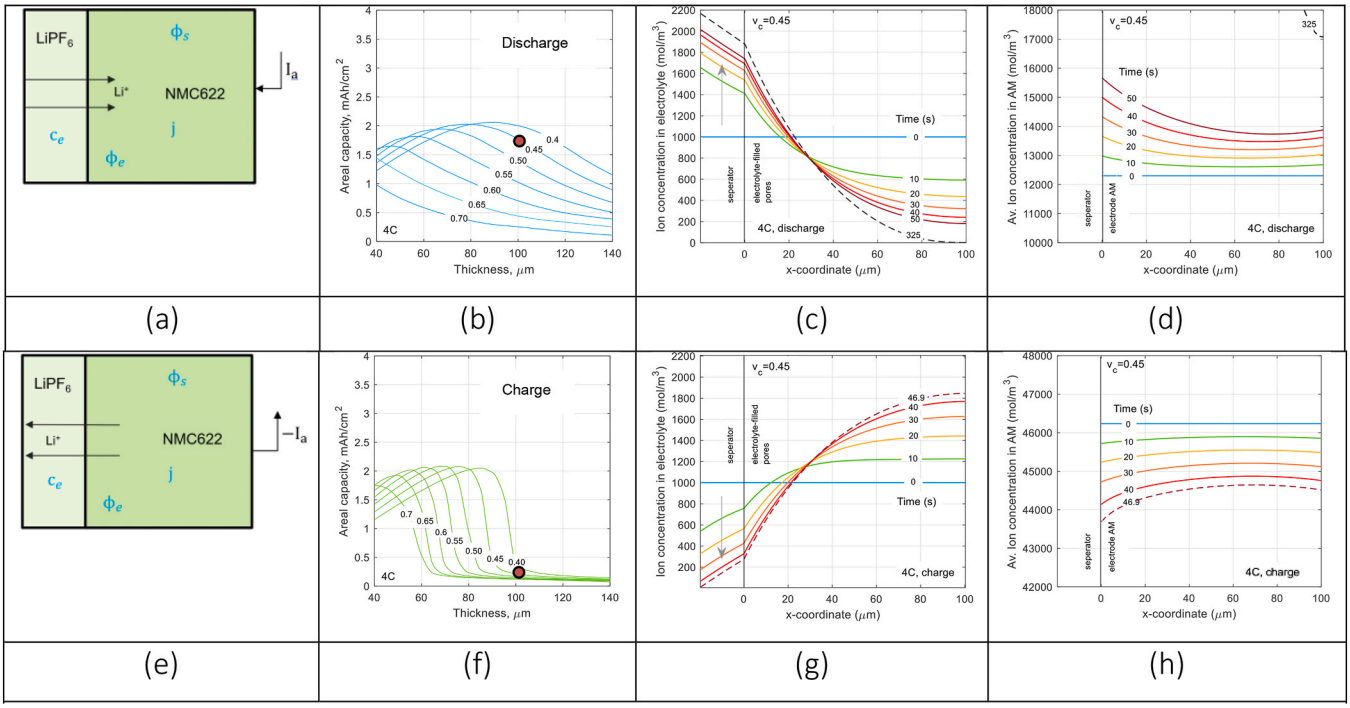

Fig. 1. Half-cell configuration with NMC622 cathode under (a) 4C-discharge (lithiation) and (e) 4C-charge (de-lithiation) showing the direction of Li ion motion into and out of the electrode under applied current density, $\mathbf{I_a}$. The variation of areal capacity with electrode thickness for a range of AM volume fractions are shown for lithiation (b) and de-lithiation (f). As an example of the asymmetry between charge and discharge, the red maker identifies an electrode with AM volume fraction, $\mathbf{v_c = 0.45}$ and electrode thickness, $\mathbf{L_c = 100\ \mu m}$. For this example, (c) and (g) show the electrolyte concentration profiles across the separator and electrolyte-filled pores of the electrode in discharge and charge respectively at different (dis)charge times. Dashed curves represent electrolyte concentration profile at cut-off voltage, 3V. Finally, the average Li concentration profiles in the AM particles of the NMC622 cathode are shown in (d) and (h) for discharge and charge at 4C. (For interpretation of the references to colour in this figure legend, the reader is referred to the Web version of this article.)

Li-ion transport (de-intercalation), the capacity-thickness curves show similar trends but with a qualitatively different curve shape. Despite similar areal capacity maxima at lower electrode thicknesses in both the charge and discharge case (~2 mAh/cm^2), the areal capacity drops much more rapidly with increasing electrode thickness in the charge case. As in the discharge case, the drops occur at increasingly lower thicknesses as the AM volume fraction increases, but this time, reaching extremely low areal capacity rapidly, soon after peaking. This disparity in electrode performance based only on the direction of the lithium into or out of the electrode at high rates defines an asymmetry in electrode performance which is also observed in real electrodes [33,43]. As well as exploring the capacity-rate capability trade-off, the model can identify the origin of the charge/discharge assymetry, as described in the next section.

3.2. The asymmetry of electrode performance in high-rate charge or discharge

The continuum model shows the evolution of the initially uniform Li ion concentration in the electrolyte (set at 1M), both within the electrode pores and in the separator region, once current flows. The general phenomenology can be understood by studying one example (v_c = 0.45, positive electrode thickness, L_c = 100 μm, 4C) in more detail (Fig. 1c & g). During discharge (lithiation, Fig. 1c), the bulk electrolyte in the separator region was flooded with lithium ions from the counter electrode, with the concentration gradually increasing as time elapsed. As a result, crucially, the ionic conductivity in this region always remained high. Li ions were then stored in the AM as electrons were injected. An increasing concentration gradient was established across the electrode thickness due to the variation between liquid and solid phase diffusion. Average ion concentration in the AM increased accordingly, increasing faster closer to the separator side compared to the current collector side (Fig. 1d). Discharge was terminated at cut-off voltage after 325 s when the electrolyte concentration in the electrode pores reached zero.

In contrast, during high C-rate charge (positive electrode delithiation), the lithium ions in the bulk electrolyte were rapidly depleted as they moved to the counter electrode, since the diffusion of lithium out of the NMC particles is a slower process. This depletion of Li-ions in the electrolyte relatively quickly led to complete ionic insulation (Fig. 1f) that suddenly terminated the ion transport process when the concentration at the counter electrode surface reached zero. Ultimately, the voltage dropped rapidly due to increased overall resistance and higher ohmic overpotentials and the same voltage cut-off (as in the discharge case) was reached after just 47 s, resulting in low useful charged capacity [33]. For the 100$\mu m-$ thick electrode of v_c = 0.45, the capacity at termination was far less in charge compared to the discharge (Fig. 2b and f). Recognising the cause of this charge-discharge asymmetry in Li lithiation and delithiation is essential to the discussions of Sections 3.4 and 3.5, where the performance space of the positive and negative electrodes are explored. Electrolyte ion depletion or flooding as a consequence of the limitation in electrolyte diffusion in the low volume fraction of electrolyte pores is one key limitation to battery fast charging or discharging and constitutes an active research field [44–47]. Capacity curves during charge and discharge at low C-rates are comparably symmetric.

3.3. Electrode performance map sampling

The performance maps of half-cell electrodes were explored to determine optimal electrode parameters under charge and discharge. Using the continuum half-cell NMC622 configuration of Fig. 1a under discharge (electrode lithiation) of electrode thickness, L_c, and AM volume fraction, v_c, a full factorial sampling of both variables was

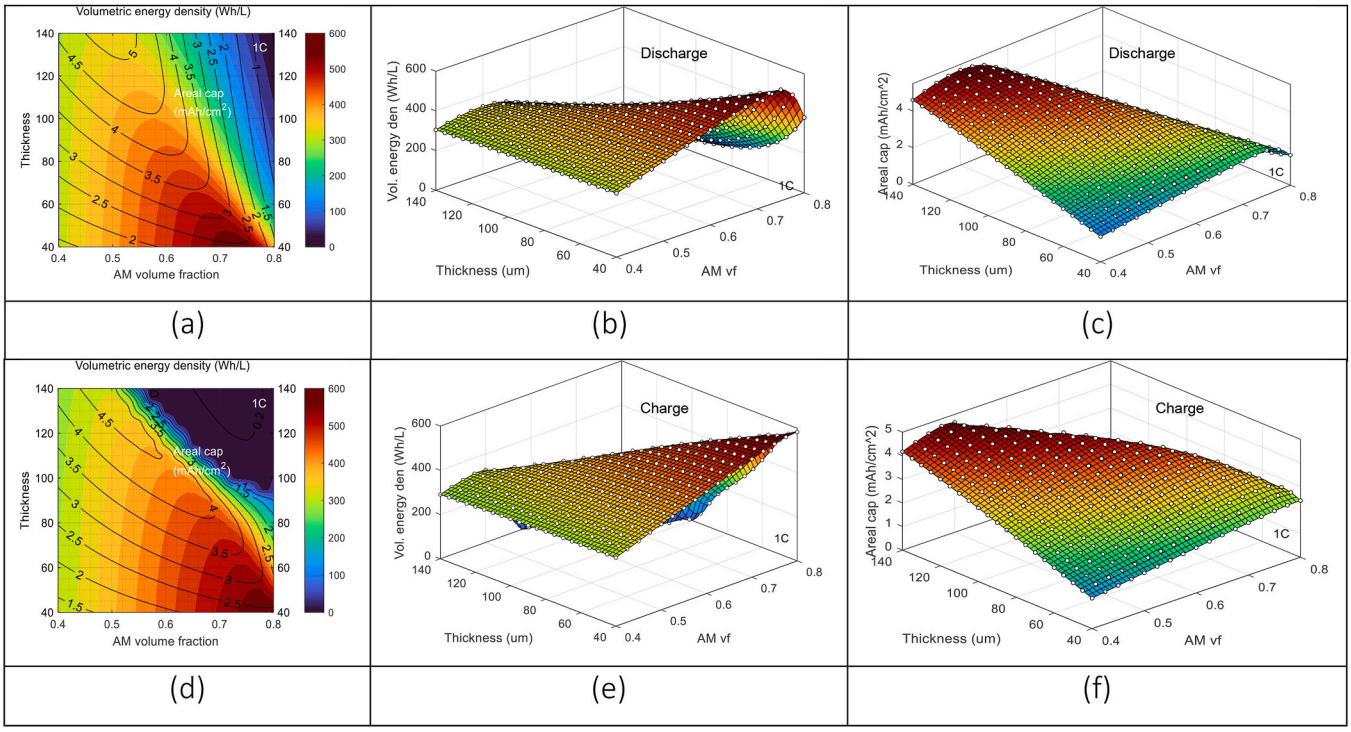

Fig. 2. (a) Volumetric energy density (colour map) with superposed areal capacity contour curves (black) mapped in the electrode thickness and volume fraction plane, 1C discharge (cathode lithiation), (b) and (c) show interpolation functions through sampled points for the volumetric energy density and areal capacity respectively, further emphasizing that peaks for both performance metrics do not coincide. (d) Variation of volumetric energy density (colour map) and areal capacity (black contour curves) with electrode thickness and volume fraction at 1C charge (cathode de-lithiation), (e) and (f) show interpolation functions through simulated points for the volumetric energy density and areal capacity respectively. Drop-off in capacity and volumetric energy density (at the top right) is a consequence of electrolyte ion depletion. (For interpretation of the references to colour in this figure legend, the reader is referred to the Web version of this article.)

conducted at a discharge rate of 1C. The model parameters and material properties were kept consistent with those used for validating the models (Tables 1 and 2 in the ESI), and for previous work (on positive electrodes) [42]. The range of the AM volume fraction modelled (0.4–0.8) was selected as reasonable and representative of real slurry-cast electrodes. In addition, above $v_c = 0.8$, the connectivity of the porosity is no longer guaranteed, ion diffusion through the electrolyte-filled pores becomes significantly limited and percolation effects are no longer captured correctly by porous electrode theory [48]. The range of electrode thicknesses 40 to 140 μm is also reasonable and typically manufactured in industry. At each sampling point, the volumetric energy density (in Wh L^{-1}) and areal capacity (in mAh/ cm^2) were determined.

Increasing AM volume fraction and/or electrode thickness increases the theoretical capacity of the electrode but the useful capacity and volumetric energy density is limited at practical discharge rates (Fig. 2). In fact, regions of high electrode thickness and AM volume fraction (top-right region of Fig. 2a) show poor performance values for both metrics. There are combinations of electrode thickness and AM volume fraction that yield high volumetric energy density (i.e., 40 µm, ~ 0.72, respectively). However, these combinations do not yield the highest areal capacities. Highest areal capacity is attained elsewhere in the map (i.e., 140 µm, ~ 0.5 respectively) where the electrode is thick and the porosity is high enough to support efficient ion transport. Though the performance map shows where these metrics are highest and can be useful for exploring each performance metric separately, it does not directly indicate the optimal electrode parameters to satisfy both metrics simultaneously. In fact, interpolation functions for volumetric energy density and areal capacity, derived from performance sampling data, emphasise the non-coincidence of the performance metrics (Fig. 2b and 3c). These interpolation functions can be readily evaluated to determine the performance metrics given specific thicknesses and AM volume fraction values for an NMC622 electrode.

With identical electrode parameters and material properties, the same positive electrode under charge (cathode delithiation) yields a different performance map (Fig. 2d–f). A sudden drop-off in areal capacity and volumetric energy density leads to a region of intermediate to high thickness and AM volume fraction values with very low performance (top-right corner of Fig. 2d). This abrupt decline is due to the depletion of ions in the electrolyte during high C-rate charging of this positive electrode, as discussed in Section 3.2. Ion depletion in the electrolyte leads to poor ionic conductivity that severely limits cell useful capacity. Before this onset, the performance metrics are quite similar in both charge and discharge. This ionic insulation effect in the electrolyte is an indirect consequence of slow solid phase diffusion at high C-rates, since the supply of Li^+ fails to keep up with the depletion of the electrolyte. Diffusivity in the electrolyte is several orders of magnitude higher than in the AM particles ($\sim 10^{-9}\, m^2/s$ in the electrolyte and $\sim 10^{-13}\, m^2/s$ in AM particles) [27,49]. Ultimately, the severe concentration gradients at the electrode surface result in high concentration overpotentials that lead to the plunge in potential and early termination of the de-lithiation process. The equivalent effect occurs on the negative electrode during de-lithiation, corresponding in this case to discharge.

When the performance space is sampled for the graphite anode (Fig. 3) at the same current density, the maximum accessible volumetric energy density and areal capacity values are lower, indicating that the graphite electrode is more limiting than the NMC622 electrode. The map shows that the highest volumetric energy density occurs for the thinnest electrode sampled but at an intermediate AM volume fraction. Compared to the cathode, higher porosities are required at the same electrode thickness to yield the best energy density within the sampled space. Similar to the cathode, the highest areal capacities also occur for the thickest electrodes, however, requiring the highest porosities (lowest AM volume fraction) to facilitate the capacity delivery.

These opposing trends reflect fundamental transport limitations at practical C-rates. Maximum areal capacity requires thick electrodes but with high porosity (low AM volume fraction) to provide sufficient Li-ion transport to ensure reasonable material utilisation despite the long ionic conduction paths. In contrast, maximum volumetric energy density is achieved in thin electrodes where short diffusion distances minimise concentration and kinetic overpotentials for near-complete AM utilisation but requiring only moderate porosity (AM volume fraction) for adequate ionic conductivity. The graphite anode exhibits more pronounced limitations due to slower solid-phase diffusion, shifting optima toward higher porosities relative to NMC622.

3.4. Full-cell electrode capacity balancing for high performance

The performance maps of Figs. 2 and 3 offer an opportunity to assemble matched electrodes for a high performance full-cell configuration. However, they don't indicate where in the performance map an optimal design lies or provide precise electrode thicknesses and AM volume fraction values but rather, are only a visualisation of the performance space. In this section, the performance evaluations for each electrode design are combined to inform optimal choices of electrode parameters for a 1C charge case. The framework can be extended to the discharge case at different charge rates as well as to other electrode materials.

The AM-Vf performance maps (Fig. 2d–f and 3a-c) were replotted in the areal capacity-volumetric energy density plane (Fig. 4), providing a perspective that facilitates an optimal design choice under the charge case. Fundamentally, high volumetric energy density maximises the extent to which the intrinsic performance of the AM is used, minimises

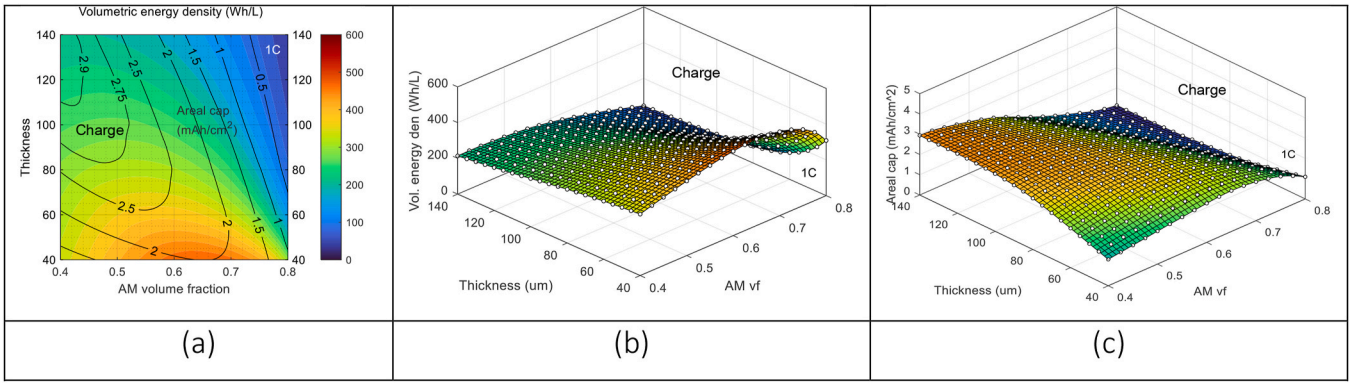

Fig. 3. (a) Variation of volumetric energy density (colour map) and areal capacity (black contour curves) with electrode thickness and volume fraction at 1C charge (negative electrode lithiation), (b) and (c) show interpolation functions through simulated points for the volumetric energy density and areal capacity respectively. (For interpretation of the references to colour in this figure legend, the reader is referred to the Web version of this article.)

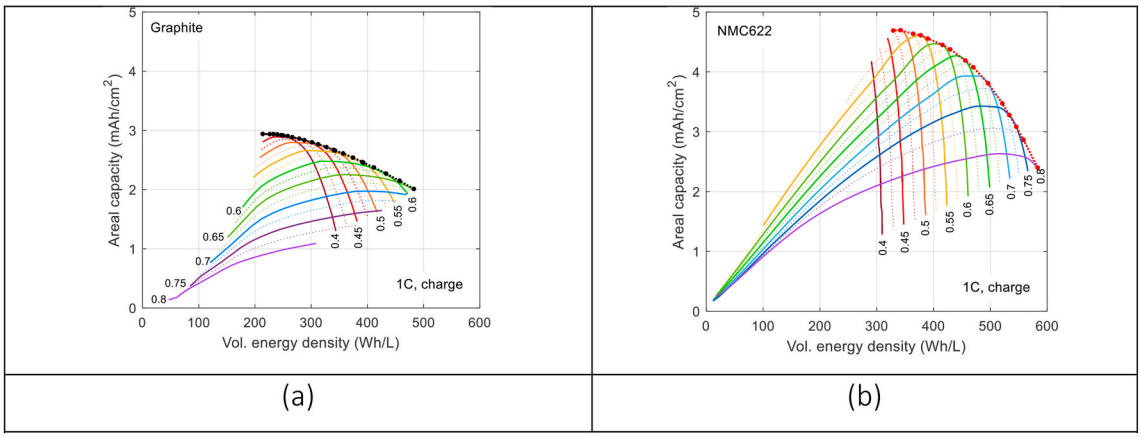

Fig. 4. Curve plots indicating constant AM volume fraction for increasing thickness of the (a) negative electrode and (b) positive electrode during a 1C charge process (i.e. negative electrode lithiation and positive electrode de-lithiation). The best performing electrode designs are indicated with black and red markers along a Pareto. Designs along this Pareto yield the best combinations of areal capacity and vol. energy density for candidate high-performing electrodes. (For interpretation of the references to colour in this figure legend, the reader is referred to the Web version of this article.)

AM costs and minimises electrolyte weight and cost penalties. High areal capacity minimises the cost and performance penalties associated with other cell components (especially current collectors) and reduces manufacturing cost.

For the negative electrode, where lithiation is occurring, the constant curves of AM volume fraction ranging from 0.4 to 0.8 show that varying electrode thickness can improve areal capacity to a certain limit, provided the porosity is sufficiently high to facilitate efficient ion transport. The peak areal capacity reached decreases with increasing AM volume fraction as the porosity diminishes (Fig. 4a). For $v_a > 0.7$ at this charge rate, increasing electrode thickness does not improve areal capacity as material utilisation degrades due to inefficiencies in ion transport. For all volume fractions, increasing electrode thickness (along each curve) always results in lower volumetric energy density as an increasing proportion of AM is inaccessible at the 1C charge rate. For the simulated electrode thicknesses, a peak volumetric energy density is attained (e.g. $v_a \approx 0.65$ for $L_a = 40$ μm) beyond which any further increases in AM volume fraction only degrade energy density (Fig. 5a). The black dotted curve of Fig. 4a represents the Pareto front of optimal designs for the graphite electrode along which the best possible trade-offs between the two performance objectives exist. Along the Pareto, alternatives range from electrode designs of highest areal capacity (left corner) to designs of highest volumetric energy density (right corner). The designs with the highest areal capacities are generally thick electrodes of low AM volume fraction (high porosity) as shown in Fig. 4a, facilitated by efficient ion transport and high material utilisation. The designs with the highest volumetric energy densities are thin electrodes with sufficient porosity to assist ion transport (intermediate AM volume fraction). Where porosities are low, volumetric energy density is comparatively low as shown in Fig. 5a. The optimal designs lying along the Pareto have been projected onto Fig. 5a to show the corresponding optimal electrode thicknesses. An electrode design positioned along this Pareto presents an opportunity for optimal full-cell design, provided electrode capacity balancing requirements can be satisfied.

In the positive electrode where de-lithiation occurred during charging, the peak areal capacity delivered was also limited (Fig. 4b). At lower AM volume fraction ($v_c < 0.48$), increasing electrode thickness for the simulated range always results in an increased capacity delivered. However, for $v_c > 0.48$, a peak areal capacity is reached with a much steeper drop in capacity (compared to the graphite electrode). This drop in capacity at the 1C charge rate is associated with the depletion of ions in the electrolyte causing a loss of ionic conductivity

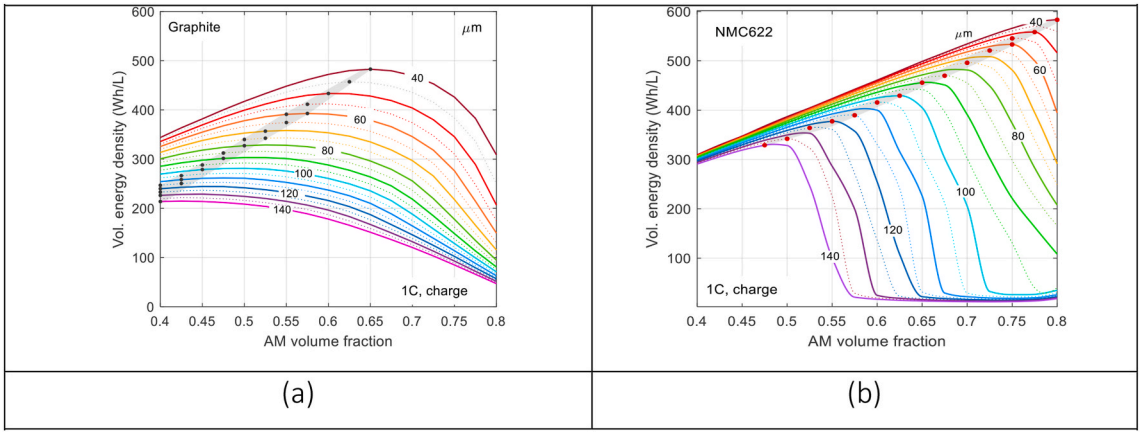

Fig. 5. Curve plots of constant electrode thickness showing variation of vol. energy density with AM volume fraction for the (a) negative electrode and (b) positive electrode during a 1C charge process (i.e. negative electrode lithiation and positive electrode de-lithiation). Increasing AM volume fraction increases vol. energy density, reaching a peak at an optimal AM volume fraction for each thickness. This optimal AM volume fraction shifts to the left as the electrode thickness increases to indicate a requirement for higher porosity to reach optimal material utilisation as the electrode thickness increases. High-performing electrode designs on the Pareto (i.e. best performing explicitly simulated designs) of Fig. 6a and b are shown for the negative and positive electrode in black and red markers respectively. (For interpretation of the references to colour in this figure legend, the reader is referred to the Web version of this article.)

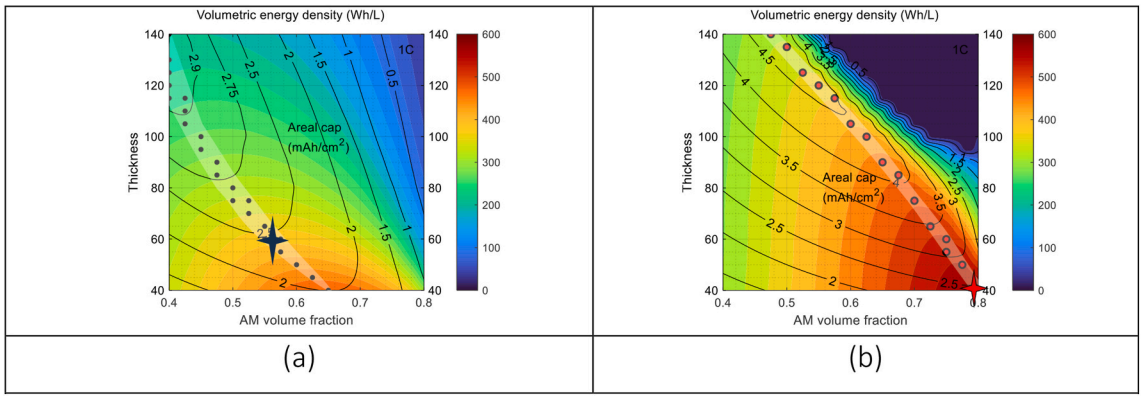

Fig. 6. High-performance electrode designs from the Pareto projected unto performance maps for (a) NMC electrode and (b) Graphite electrode showing high performance parameter combinations.

and early termination of the charge process, as discussed in Section 3.3. This process is not a problem at the negative electrode (during charging) since the electrolyte is flooded with ions and material utilisation is limited directly by the slow solid phase diffusive processes in the graphite particles. The peak areal capacity attained, here, for a given thickness, increases with AM volume fraction reaching a peak at about $v_c = 0.48$, after which it decreases with increasing AM volume fraction (Fig. 4b). However, unlike the graphite electrode where a peak volumetric energy density is reached at an intermediate AM volume fraction, the highest vol. energy density coincides with the highest simulated AM volume fraction, $v_c = 0.8$. For all AM volume fraction values, the thinnest electrode always delivered the highest vol. energy density. Whilst, in principle, a further improvement in performance might be obtained at higher AM volume fraction, the upper limit on the simulated AM volume fraction range is already high in practical terms, typical of manufactured electrodes. This practical limitation also corresponds to a computational limitation, since the porous electrode theory begins to break down, as porosity tends to zero; both limits mean that any further increase will be at most modest. Nevertheless, the constant AM volume fraction curves of Fig. 4 confirm that negative electrode is under more severe solid phase diffusive limitations than the positive electrode, as shown by the more upright constant AM volume fraction lines of the positive electrode at low AM volume fractions. The peak areal capacities and volumetric energy densities achieved by the negative electrode are also lower than those of the positive electrode for the same charge rate. Like the negative electrode, the red markers lying on the Pareto in Fig. 4b represent the optimal NMC622 electrode designs ranging from those with the highest areal capacity (left corner) to the designs with the highest vol. energy density (right corner). A positive electrode design along this Pareto, satisfying the requirement for balanced areal capacity, presents an opportunity for optimal full-cell design.

The high-performing designs on the Pareto can be summarised on overall areal capacity-volumetric energy density performance maps (Fig. 6(a) and (b)). These high-performing design points are shown to lie along the crest of both performance metrics. Since the ultimate objective of the framework is to match capacities of the positive and negative electrode in such a way as to construct a full-cell configuration with the best combination of areal capacity and volumetric energy density, Fig. 7 shows the upper and lower bounds for feasible capacity matching. Each point represents an electrode design point. Suboptimal designs have been greyed out to highlight the optimal designs along the Paretos. The optimal cathode design thickness and AM volume fraction are such that $40\ \mu m < L_c < 52\ \mu m$ and $0.76 < v_c < 0.8$ respectively. Equivalent ranges for the negative electrode parameters are $56\ \mu m < L_a < 140\ \mu m$ and $0.4 < v_a < 0.58$ respectively. The upper limit on areal capacity for the full cell is bounded by the achievable capacity of the negative electrode as the curve peaks at ~2.94 mAh/cm^2. To improve the full cell capacity any further, a negative electrode with higher capacity or higher

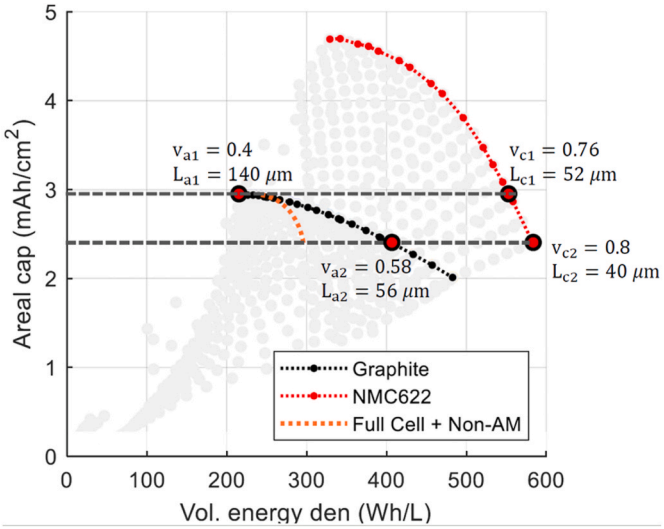

Fig. 7. Scatter plot of superposed simulated points for both electrodes. Non-optimal design data points have been greyed out to highlight high-performing Pareto points for the positive electrode (red unbounded markers) and for the negative electrode (black markers). The black dashed lines correspond to the upper and lower bounds of areal capacity that can be accommodated for a full-cell configuration using these electrodes. The electrode parameters at these limits are indicated (red bounded markers) along the Pareto. N/P ratio is chosen as unity to demonstrate capacity balance. The areal capacity – cell volumetric energy density plot is shown for a full-cell configuration demonstrating the penalty for parasitic (non-active) components of **20 μm** thick current collectors and the electrolyte-filled **20 μm** thick separator (orange curve). (For interpretation of the references to colour in this figure legend, the reader is referred to the Web version of this article.)

diffusion coefficient must be employed. The lower limit is bounded by the simulated thickness and AM volume fraction limits of the cathode, beyond which practical electrode manufacture becomes challenging and the porous electrode theory breaks down. This argument is outlined assuming an exact areal capacity match between the two electrodes, to simplify the use of horizontal, matched areal capacity tie lines in the diagram; the small negative electrode excess used typically in practice (N/P > 1) to limit plating, will not substantively change the conclusions. Regarding the effects of our model assumptions such as uniform spherical particles, the heterogeneity in real electrodes leads to regions of relative inaccessibility, due to larger particle size or pore blocking by binder, that culminates in reduced volumetric and areal energy density

by some factor. The position of the abrupt cut-off during delithiation will be more severe, due to reduced accessible lithium supply. However, qualitatively, the trends will be similar, as long as lithium plating on larger particles is avoided. The position of the optima, and hence the Pareto fronts will likely not move significantly, as they are not close to the cut off, however, absolute cell performance will be slightly reduced.

A full-cell design includes other non-active materials and components that constrain practical volumetric energy density. Components such as the current collectors and separator increase total mass and volume of the cell, without contributing to energy storage capacity. The orange dashed curve of Fig. 7 schematically illustrates the effect of these considerations on the cell volumetric energy density, normalised by the volumes of all components (including non-active components):

$$V_{cell} = \frac{V_a L_a + V_c L_c}{L_{cca} + L_a + L_{sep} + L_c + L_{ccc}} \quad (1)$$

where V and L denote volumetric energy density and component thickness, respectively, and the subscripts are a for negative electrode, c for positive electrode, sep for separator and cca and ccc for current collectors of the negative and positive electrode respectively. Clearly, the exact effect depends on current collector and separator thicknesses, but qualitatively, it's clear that the effect is to locate the optimum more firmly within the band already highlighted.

At the most critical condition, where the highest thicknesses in practice have been used for the non-active components to represent the most severe parasitic penalties, the cell volumetric energy density is seen to approach a peak volumetric energy density value, defining an optimal areal capacity for the design (See orange dashed line in Fig. 7). Below the minimum areal capacity for this configuration, limited by the minimum realistic porosity of the cathode, the full-cell volumetric energy can be expected to perform no better. The best areal capacity for the full-cell design that maximises volumetric energy density is ~2.47 mAh/cm^2, occurring at the lower bound of the areal capacity. The corresponding optimal electrode parameters for the negative and positive electrodes are summarised in Table 1.

The optimal parameters are indicated as the black and red stars on the performance maps of Fig. 6a and (b) for the negative and positive electrodes respectively.The parameters again show that the negative electrode limits the highest areal capacity attainable, requiring lower AM volume fraction (more porosity) to fulfil the same capacity at the same charge rate compared to the positive electrode. The positive electrode being less limiting favours higher AM volume fraction. However, the highest volumetric energy density for a full-cell configuration, at this charge rate, is limited by the lowest porosity of the positive electrode attainable.

The results for an optimal full-cell design obtained are reasonable. The thickness and porosity of the negative and positive electrodes of a commercially available LG M50 cell are 85μm, 24.9% and 75.6μm, 33.5% respectively [50]. The values here are for porosity rather than AM volume fraction but correspond effectively to AM around 65 % and 56 % (if we assume ~10 % non-AM) for the negative and positive electrodes respectively, which is not unreasonable compared to the simulated range. It is operated on a nominal voltage of 3.63V and charge rate of 0.3C (1455mA) but is designed to withstand charge at a maximum voltage and current of 4.2V and charge rate of 0.7C (3395mA). The cell capacity has been balanced to an N/P ratio of 1.1. The LG M50 has been chosen for comparison based on its similar chemistry and components. However, its nominal operational parameters show that its electrodes have been balanced for lower current densities. Regardless, interesting qualitative inferences can be drawn from its comparison. Like the LG M50, our negative electrode is thicker than the positive electrode, albeit that both electrodes in our design have lower thicknesses than those of the LG M50, owing to the higher current density for which it's designed; similarly our negative electrode has higher porosity to deliver capacity at higher current density. To match the capacity of our negative electrode, our positive electrode porosity can be lower than the LG M50's.

Table 1
Electrode parameters for NMC622/Graphite full-cell configuration.

Component	Thickness (μm)	AM vol. fraction	Porosity	Solid density (g/cm^3)
Negative current collector (Copper)	20	–	–	8.96
Negative electrode (Graphite)	59.8	0.562	.34	2.26
Separator	20	–	–	0.9
Positive electrode (NMC622)	41.3	0.79	0.11	4.61
Positive current collector (Aluminium)	20	–	–	2.7

4. Summary and conclusion

A rational strategy for electrode capacity balancing of high-performance cells has been presented for fast charging and discharging applications. The presence of overpotentials at intermediate/high current densities makes the balancing process non-trivial since candidate electrodes for a full-cell configuration behave differently under high-rate charge or discharge. Consequently, using validated half-cell models for a positive and negative electrode, a high-performance full-cell configuration with high areal capacity and energy density is determined. By exploring the performance field of each electrode and determining a Pareto-front of high-performing designs, capacity balancing informs the choice of an optimal design. The study also demonstrates that electrolyte depletion or flooding, a consequence of the slow solid-phase ion transport, is a key limitation to fast charging or discharging, which occurs asymmetrically. Though an NMC622 positive electrode and graphite negative electrode have been used to demonstrate the strategy, the method can be applied to other chemistries and current densities. Ultimately, in the present chemistry, the graphite anode is the primary limitation to the performance of a full-cell configuration, particularly at these elevated charge and discharge rates. Therefore, enhancing the anode performance should be a priority in future research.

The results of this study also demonstrate how modelling can accelerate battery design at low cost. The comprehensive performance maps of volumetric energy density versus areal capacity are combined to uncover a Pareto-optimal front that identifies electrode pairs achieving maximal material utilisation, while quantifying the interplay of thickness, porosity, and rate-dependent kinetics across both electrodes. This approach bridges the gap between theoretical and practical cell design and provides actionable guidelines for manufacturing higher-capacity, fast-charging batteries, paving the way for accelerated innovation beyond empirical trial-and-error. Data generated from this strategy could be formulated into an interactive user toolkit for a range of battery chemistries and current densities to yield high-performance battery design blueprints used by manufacturers, providing inspiration for further research work. Though simulations have not incorporated degradation mechanisms, the results are valid and useful at intermediate C-rate. The objective of our study was to develop a framework to determine optimal electrode parameters satisfying multiple objectives. The results have been compared with one commercial cell to illustrate the process of comparison and the relevance of our design maps. These maps allow users to read off cases relevant for their use and to appreciate the trade-offs highlighted in our study that are relevant widely. It is more appropriate to employ the tools on specific systems than to attempt comprehensiveness. However, in future works, we will upgrade our continuum models to capture degradation mechanisms such as lithium plating and extend the framework to other laboratory-scale full cells and data sets. Finally, the results have been presented in the volumetric space, suited to space-limited applications such as in portable or

wearable devices. The process is conveniently agnostic towards the details of other cell components. But where such details are known, the results can also be extended to the gravimetric space to target weight-critical applications such as in electrified transport where the cell non-active materials such as the electrolyte in the pore network of the electrode, separator and current collectors present severe limitations to gravimetric performance. The detailed quantitative analysis also provides a more general, intuitive picture of the limitations faced in battery design.

CRediT authorship contribution statement

Chikwesiri Imediegwu: Writing – original draft, Visualization, Software, Methodology. **Milo S.P. Shaffer:** Writing – review & editing, Supervision, Funding acquisition. **Mary P. Ryan:** Supervision, Funding acquisition. **Ajit Panesar:** Writing – review & editing, Supervision, Methodology, Funding acquisition.

Declaration of competing interest

The authors declare that they have no known competing financial interests or personal relationships that could have appeared to influence the work reported in this paper.

Acknowledgments

The authors acknowledge the funding support of Shell Global Solutions International B.V. and the contributions from Nicola Menegazzo (Shell), Prof. Magda Titirici, Prof. Ifan Stephens and all other collaborators on the NanoBat project at Imperial College London.

Appendix A. Supplementary data

Supplementary data to this article can be found online at https://doi.org/10.1016/j.jpowsour.2025.239174.

Data availability

Data will be made available on request.

References

[1] H. Wu, Z. Xie, Y. Wang, C. Lu, Z. Ma, Modeling diffusion–induced stress on two-phase lithiation in lithium-ion batteries, Eur. J. Mech. Solid. 71 (Sept. 2018) 320–325, https://doi.org/10.1016/j.euromechsol.2018.04.005.
[2] G. Mu, S. Agrawal, P. Sittisomwong, P. Bai, Impacts of negative to positive capacities ratios on the performance of next-generation lithium-ion batteries, Electrochim. Acta 406 (Feb. 2022) 139878, https://doi.org/10.1016/j.electacta.2022.139878.
[3] F. Brosa Planella, et al., A continuum of physics-based lithium-ion battery models reviewed, Prog. Energy 4 (4) (Oct. 2022) 042003, https://doi.org/10.1088/2516-1083/ac7d31.
[4] J.P. Pender, et al., Electrode degradation in lithium-ion batteries, ACS Nano 14 (2) (Feb. 2020) 1243–1295, https://doi.org/10.1021/acsnano.9b04365.
[5] Y. Yang, et al., Edge-surface-inter carbon nanoarchitecture on silicon, ACS Nano 19 (17) (May 2025) 16597–16610, https://doi.org/10.1021/acsnano.5c00371.
[6] C. Huang, M. Dontigny, K. Zaghib, P.S. Grant, Low-tortuosity and graded lithium ion battery cathodes by ice templating, J. Mater. Chem. A 7 (37) (2019) 21421–21431, https://doi.org/10.1039/C9TA07269A.
[7] C. Huang, et al., 3D correlative imaging of lithium ion concentration in a vertically oriented electrode microstructure with a density gradient, Adv. Sci. 9 (16) (May 2022) 2105723, https://doi.org/10.1002/advs.202105723.
[8] C.-S. Kim, K.M. Jeong, K. Kim, C.-W. Yi, Effects of capacity ratios between anode and cathode on electrochemical properties for lithium polymer batteries, Electrochim. Acta 155 (Feb. 2015) 431–436, https://doi.org/10.1016/j.electacta.2014.12.005.
[9] Y. Abe, S. Kumagai, Effect of negative/positive capacity ratio on the rate and cycling performances of LiFePO4/graphite lithium-ion batteries, J. Energy Storage 19 (Oct. 2018) 96–102, https://doi.org/10.1016/j.est.2018.07.012.
[10] Z. Chen, et al., Effect of N/P ratios on the performance of LiNi0.8Co0.15Al0.05O2||SiO/Graphite lithium-ion batteries, J. Power Sources 439 (Nov. 2019) 227056, https://doi.org/10.1016/j.jpowsour.2019.227056.
[11] C. Cheng, R. Drummond, S.R. Duncan, P.S. Grant, Extending the energy-power balance of Li-ion batteries using graded electrodes with precise spatial control of local composition, J. Power Sources 542 (Sept. 2022) 231758, https://doi.org/10.1016/j.jpowsour.2022.231758.
[12] C. Cheng, R. Drummond, S.R. Duncan, P.S. Grant, Micro-scale graded electrodes for improved dynamic and cycling performance of Li-ion batteries, J. Power Sources 413 (Feb. 2019) 59–67, https://doi.org/10.1016/j.jpowsour.2018.12.021.
[13] C. Cheng, R. Drummond, S.R. Duncan, P.S. Grant, Extending the energy-power balance of Li-ion batteries using graded electrodes with precise spatial control of local composition, J. Power Sources 542 (Sept. 2022) 231758, https://doi.org/10.1016/j.jpowsour.2022.231758.
[14] X. Liu, Y. Zeng, W. Yuan, G. Zhang, H. Zheng, Z. Chen, Advances in multi-scale design and fabrication processes for thick electrodes in lithium-ion batteries, Energy Rev. 3 (2) (June 2024) 100066, https://doi.org/10.1016/j.enrev.2023.100066.
[15] C. Qi, et al., Suitable thickness of carbon coating layers for silicon anode, Carbon 186 (Jan. 2022) 530–538, https://doi.org/10.1016/j.carbon.2021.10.062.
[16] Z. Song, et al., Development of advanced anodes for solid-state lithium batteries, Mater. Today 88 (Sept. 2025) 1005–1027, https://doi.org/10.1016/j.mattod.2025.06.041.
[17] P.S. Grant, et al., Roadmap on Li-ion battery manufacturing research, JPhys Energy 4 (4) (Oct. 2022) 042006, https://doi.org/10.1088/2515-7655/ac8e30.
[18] M.D. Radin, et al., Narrowing the gap between theoretical and practical capacities in li-ion layered oxide cathode materials, Adv. Energy Mater. 7 (20) (Oct. 2017) 1602888, https://doi.org/10.1002/aenm.201602888.
[19] G. Zan, et al., An approaching-theoretical-capacity anode material for aqueous battery: hollow hexagonal prism Bi2O3 assembled by nanoparticles, Energy Storage Mater. 28 (June 2020) 82–90, https://doi.org/10.1016/j.ensm.2020.02.027.
[20] Z. Du, D.L. Wood, C. Daniel, S. Kalnaus, J. Li, Understanding limiting factors in thick electrode performance as applied to high energy density Li-ion batteries, J. Appl. Electrochem. 47 (3) (Mar. 2017) 405–415, https://doi.org/10.1007/s10800-017-1047-4.
[21] C. Heubner, et al., Understanding thickness and porosity effects on the electrochemical performance of LiNi0.6Co0.2Mn0.2O2-based cathodes for high energy Li-ion batteries, J. Power Sources 419 (Apr. 2019) 119–126, https://doi.org/10.1016/j.jpowsour.2019.02.060.
[22] L. Bläubaum, F. Röder, C. Nowak, H.S. Chan, A. Kwade, U. Krewer, Impact of particle size distribution on performance of lithium-ion batteries, Chemelectrochem 7 (23) (Dec. 2020) 4755–4766, https://doi.org/10.1002/celc.202001249.
[23] Z. Wang, et al., Perspectives on strategies and techniques for building robust thick electrodes for lithium-ion batteries, J. Power Sources 551 (Dec. 2022) 232176, https://doi.org/10.1016/j.jpowsour.2022.232176.
[24] M. Ali, C. Da Silva, C. Amon, Multiscale modelling methodologies of lithium-ion battery aging: a review of Most recent developments, Batteries 9 (9) (Aug. 2023) 434, https://doi.org/10.3390/batteries9090434.
[25] Z. Ma, H. Wu, Y. Wang, Y. Pan, C. Lu, An electrochemical-irradiated plasticity model for metallic electrodes in lithium-ion batteries, Int. J. Plast. 88 (Jan. 2017) 188–203, https://doi.org/10.1016/j.ijplas.2016.10.009.
[26] M.J. Lain, J. Brandon, E. Kendrick, Design strategies for high power vs. high energy lithium ion cells, Batteries 5 (4) (Oct. 2019) 64, https://doi.org/10.3390/batteries5040064.
[27] A.A. Wang, et al., Review of parameterisation and a novel database (LiionDB) for continuum Li-ion battery models, Prog. Energy 4 (3) (July 2022) 032004, https://doi.org/10.1088/2516-1083/ac692c.
[28] Y. Dong, et al., Challenges and strategies of fast-charging Li-Ion batteries with a focus on Li plating, Energy Mater Adv 5 (Jan. 2024) 113, https://doi.org/10.34133/energymatadv.0113.
[29] C. Heubner, K. Nikolowski, S. Reuber, M. Schneider, M. Wolter, A. Michaelis, Recent insights into rate performance limitations of li-ion batteries, Batteries & Supercaps 4 (2) (Feb. 2021) 268–285, https://doi.org/10.1002/batt.202000227.
[30] M. Singh, J. Kaiser, H. Hahn, A systematic study of thick electrodes for high energy lithium ion batteries, J. Electroanal. Chem. 782 (Dec. 2016) 245–249, https://doi.org/10.1016/j.jelechem.2016.10.040.
[31] K. Fu, X. Li, K. Sun, P. Tan, Clarifying the limiting factor of material utilization in thick electrodes of lithium-ion batteries, J. Power Sources 591 (Jan. 2024) 233880, https://doi.org/10.1016/j.jpowsour.2023.233880.
[32] B.-S. Lee, et al., Analysis of rate-limiting factors in thick electrodes for electric vehicle applications, J. Electrochem. Soc. 165 (3) (2018) A525–A533, https://doi.org/10.1149/2.0571803jes.
[33] Michael J. Lain, E. Kendrick, Understanding the limitations of lithium ion batteries at high rates, J. Power Sources 493 (May 2021) 229690, https://doi.org/10.1016/j.jpowsour.2021.229690.
[34] Chikwesiri Imediegwu, Milo S.P. Shaffer, Mary P. Ryan, Ajit Panesar, Modelling optimum thickness and architecture for lithium-ion battery cathodes, J. Power Sources 614 (Sept. 2024) 235005, https://doi.org/10.1016/j.jpowsour.2024.235005.
[35] T. Song, Y. Chen, L. Chen, E. Kendrick, Areal capacity balance to maximize the lifetime of layered oxide/hard carbon sodium-ion batteries, J. Power Sources 624 (Dec. 2024) 235599, https://doi.org/10.1016/j.jpowsour.2024.235599.
[36] I. Jeon, W.G. Hong, S. Yoon, Y. Choi, H.J. Kim, J.-P. Kim, Safety, high-performing and effects of the N/P ratio of a solid lithium ion battery using PEGDME based polymer electrolytes, Heliyon 9 (2) (Feb. 2023) e13292, https://doi.org/10.1016/j.heliyon.2023.e13292.

[37] P. Ngatchou, A. Zarei, A. El-Sharkawi, Pareto multi objective optimization, in: *Proceedings of the 13th International Conference On, Intelligent Systems Application to Power Systems*, Arlington, IEEE, Virginia, USA, 2005, pp. 84–91, https://doi.org/10.1109/ISAP.2005.1599245.
[38] T. Beuse, M. Fingerle, C. Wagner, M. Winter, M. Börner, Comprehensive insights into the porosity of lithium-ion battery electrodes: a comparative study on positive electrodes based on LiNi0.6Mn0.2Co0.2O2 (NMC622), Batteries 7 (4) (Oct. 2021) 70, https://doi.org/10.3390/batteries7040070.
[39] Y.-J. Choi, Y.-S. Lee, J.-H. Kim, J.-S. Im, Optimization of pore characteristics of graphite-based anode for Li-Ion batteries by control of the particle size distribution, Materials 16 (21) (Oct. 2023) 6896, https://doi.org/10.3390/ma16216896.
[40] A.S. Ho, et al., 3D detection of lithiation and lithium plating in graphite anodes during fast charging, ACS Nano 15 (6) (June 2021) 10480–10487, https://doi.org/10.1021/acsnano.1c02942.
[41] W. Li, Onset of lithium plating in fast-charging Li-Ion batteries, ACS Energy Lett. 10 (4) (Apr. 2025) 1596–1604, https://doi.org/10.1021/acsenergylett.5c00322.
[42] C. Imediegwu, M.S.P. Shaffer, M.P. Ryan, A. Panesar, Modelling optimum thickness and architecture for lithium-ion battery cathodes, J. Power Sources 614 (Sept. 2024) 235005, https://doi.org/10.1016/j.jpowsour.2024.235005.
[43] Y. Chen, J. Key, K. O'Regan, T. Song, Y. Han, E. Kendrick, Revealing the rate-limiting electrode of lithium batteries at high rates and mass loadings, Chem. Eng. J. 450 (Dec. 2022) 138275, https://doi.org/10.1016/j.cej.2022.138275.
[44] C. Heubner, M. Schneider, A. Michaelis, Diffusion-limited C-rate: a fundamental principle quantifying the intrinsic limits of li-ion batteries, Adv. Energy Mater. 10 (2) (Jan. 2020) 1902523, https://doi.org/10.1002/aenm.201902523.
[45] M. Weiss, et al., Fast charging of lithium-ion batteries: a review of materials aspects, Adv. Energy Mater. 11 (33) (2021) 2101126, https://doi.org/10.1002/aenm.202101126.
[46] Z. Song, et al., Zinc-regulated hard carbon as a sodium-ion battery anode material, J. Power Sources 640 (June 2025) 236798, https://doi.org/10.1016/j.jpowsour.2025.236798.
[47] Y. Ma, et al., Advanced nanoparticle coatings for stabilizing layered Ni-rich oxide cathodes in solid-state batteries, Adv. Funct. Mater. 32 (23) (June 2022) 2111829, https://doi.org/10.1002/adfm.202111829.
[48] T. Mori, T. Ochi, K. Kitamura, Characterization of slurries for lithium-ion battery cathodes by measuring their flow and change in hydrostatic pressure over time and clarification of the relationship between slurry and cathode properties, J. Colloid Interface Sci. 629 (Jan. 2023) 36–45, https://doi.org/10.1016/j.jcis.2022.08.192.
[49] Y.K. Lee, J. Park, W. Lu, A comprehensive experimental and modeling study on dissolution in Li-Ion batteries, J. Electrochem. Soc. 166 (8) (2019) A1340–A1354, https://doi.org/10.1149/2.0111908jes.
[50] S. W. Hair, 'Beyond slurry cast: patterning of a monolithic active material sheet to form free-standing, solvent-free, and low-tortuosity battery electrodes', OPEN ACCESS.